The Astrophysical Journal Letters, 728:L39 (6pp), 2011 February 20 doi:10.1088/2041-8205/728/2/L39

THE DARK MATTER DISTRIBUTION IN A383: EVIDENCE FOR A SHALLOW DENSITY CUSP FROM IMPROVED LENSING, STELLAR KINEMATIC, AND X-RAY DATA

Andrew B. Newman[1], Tommaso Treu[2], Richard S. Ellis[1], and David J. Sand[2,3]
[1] Cahill Center for Astronomy & Astrophysics, California Institute of Technology, MS 249-17, Pasadena, CA 91125, USA
[2] Department of Physics, University of California, Santa Barbara, CA 93106, USA
[3] Las Cumbres Observatory Global Telescope Network, Santa Barbara, CA 93117, USA
Received 2010 November 15; accepted 2011 January 14; published 2011 February 1

ABSTRACT

We extend our analyses of the dark matter (DM) distribution in relaxed clusters to the case of A383, a luminous X-ray cluster at $z = 0.189$ with a dominant central galaxy and numerous strongly lensed features. Following our earlier papers, we combine strong and weak lensing constraints secured with *Hubble Space Telescope* and *Subaru* imaging with the radial profile of the stellar velocity dispersion of the central galaxy, essential for separating the baryonic mass distribution in the cluster core. Hydrostatic mass estimates from *Chandra* X-ray observations further constrain the solution. These combined data sets provide nearly continuous constraints extending from 2 kpc to 1.5 Mpc in radius, allowing stringent tests of results from recent numerical simulations. Two key improvements in our data and its analysis make this the most robust case yet for a shallow slope β of the DM density profile $\rho_{\rm DM} \propto r^{-\beta}$ on small scales. First, following deep Keck spectroscopy, we have secured the stellar velocity dispersion profile to a radius of 26 kpc for the first time in a lensing cluster. Second, we improve our previous analysis by adopting a triaxial DM distribution and axisymmetric dynamical models. We demonstrate that in this remarkably well-constrained system, the logarithmic slope of the DM density at small radii is $\beta < 1.0$ (95% confidence). An improved treatment of baryonic physics is necessary, but possibly insufficient, to reconcile our observations with the recent results of high-resolution simulations.

Key words: dark matter – galaxies: clusters: individual (A383) – gravitational lensing: strong – gravitational lensing: weak – stars: kinematics and dynamics – X-rays: galaxies: clusters

1. INTRODUCTION

The cold dark matter (CDM) paradigm has been remarkably successful at predicting the large-scale distribution of matter in the universe as well as its observed evolution from the earliest epochs to the present day (Springel et al. 2006). However, much interest has been shown in possible discrepancies that remain on small scales between its predictions and the available observations. A source of continuing puzzlement relates to the observed form of the dark matter (DM) profile seen in galaxy clusters.

Numerical simulations predict that CDM halos follow a self-similar density profile whose three-dimensional (3D) form within a scale radius r_s approaches a cusp $\rho \propto r^{-\beta}$ with an inner slope $\beta \simeq 1$–1.3 at the smallest resolved scales (e.g., Navarro et al. 1996; Ghigna et al. 2000; Diemand et al. 2005). Improved resolution has suggested modest flattening (Navarro et al. 2010), but only at very small radii. This is in contradiction to observations based on the combination of strong lensing and stellar kinematics which yielded much flatter inner slopes of $\beta \simeq 0.5$ for two well-studied clusters (Sand et al. 2008). On the other hand, a steeper $\beta = 0.92 \pm 0.04$ has been inferred in A1703 (Richard et al. 2009), possibly indicating significant scatter in the inner structure of clusters.

Recently, in Newman et al. (2009, hereafter N09), we further developed the method introduced by Sand et al. (2004, 2008) by incorporating weak lensing constraints on the large-scale mass distribution using *Subaru* imaging of A611. This removed a degeneracy between the scale radius r_s and β and led to the first measurement of the DM profile across a dynamic range in cluster-centric radius (3 kpc to 3.3 Mpc) comparable to that presently achieved in simulations. A shallow cusp with $\beta < 0.3$ (68%) was derived.

Here we make two further improvements in our methodology and apply these to A383 ($z = 0.189$). This cluster has a regular optical and X-ray morphology, a remarkably low substructure fraction, and a dominant, near-circular brightest cluster galaxy (BCG; Smith et al. 2005; Smith & Taylor 2008). Sand et al. (2004) initially studied this cluster assuming spherical symmetry but later (Sand et al. 2008) undertook a two-dimensional (2D) lensing analysis, deriving $\beta = 0.45 \pm 0.2$. In addition to removing the scale radius degeneracy discussed above, we have considerably extended the range of the stellar kinematic constraints via a deep Keck spectrum of the BCG, significantly improving our knowledge of the mass distribution on $\lesssim$30 kpc scales. Second, we use *Chandra* X-ray data to determine the line-of-sight ellipticity in the mass distribution, thereby achieving constraints on a 3D model with minimal uncertainties arising from projection effects.

We adopt a cosmology with $\Omega_\Lambda = 0.7$, $\Omega_{\rm m} = 0.3$, and $H_0 = 70\,h_{70}\,{\rm km\,s^{-1}\,Mpc^{-1}}$ throughout.

2. OBSERVATIONAL INGREDIENTS

We first discuss in turn the four observational ingredients we use to constrain the distribution of DM and baryons in A383.

2.1. Strong Lensing

Figure 1 shows the multiply imaged sources, tabulated in Sand et al. (2004, 2008) and Smith et al. (2005), which comprise the strong lensing constraints: a radial/tangential arc at $z_{\rm spec} = 1.01$ and a complex system in the southwest. In previous analyses the redshift of the latter system was unknown, but following Keck/LRIS observations in 2009 October we secured a spectroscopic redshift $z_{\rm spec} = 2.55$ for images 3C and 4C. The $n_i = 12$ images of $n_s = 4$ sources produce $2(n_i - n_s) = 16$

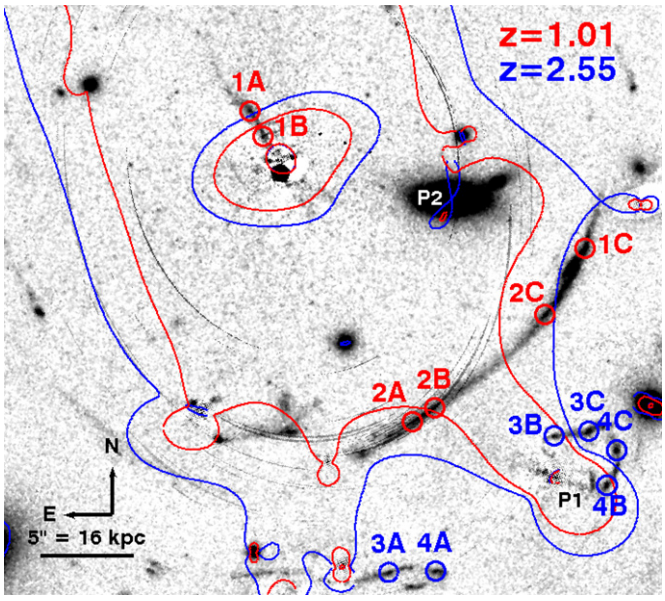

Figure 1. Strong lensing constraints: *HST*/WFC2 image in the F702W filter with the BCG and other cluster galaxies subtracted for clarity. Two families of multiple image systems with known spectroscopic redshifts, each comprising two sources, are identified in the legend. Critical lines are plotted for both source planes.

constraints. Following N09, we use `Lenstool`[4] (Jullo et al. 2007) in source plane mode for the strong lensing analysis. Consistent with earlier work, we adopt an uncertainty of $\sigma_{\rm pos} = 0\farcs5$ for the image positions to account for systematic modeling uncertainty.

2.2. Weak Lensing

The large-scale shear arising from A383 has been analyzed with multi-color imaging taken using SuprimeCam at the *Subaru* telescope. The shear was measured in R_C images taken by the authors on 2007 November 12–13 in excellent seeing of $0\farcs57$. Broadband photometry from *BViz* images in the *Subaru* archive was used with the BPZ code (Benítez 2000) to obtain photometric redshifts. The procedures closely followed those discussed by N09. From a sample of galaxies with 5σ detections in R_C, a population with $0.5 < z_b < 2$ was selected for shear measurement, yielding a surface density of 25 arcmin^{-2}. As discussed in N09, our shear measurements were calibrated using the recovery factor $m_{\rm WL} = 0.81 \pm 0.04$ based on the STEP2 simulations (Massey et al. 2007).

2.3. Stellar Kinematics

We have substantially improved the data used by Sand et al. (2008) by securing a much deeper spectroscopic exposure of the BCG (Figure 2). Earlier data yielded a stellar velocity dispersion profile $\sigma_{\rm los}(R)$ extending to $R = 5$ kpc in three spatial bins (Figure 4 of Sand et al. 2008). The present data comprise a 22.8 ks integration with Keck/LRIS taken on 2009 October 12 using the 600 mm^{-1} blue grism and the 600 mm^{-1} red grating blazed at 7500 Å. The $1\farcs5$ slit yielded a resolution of $\sigma_{\rm inst} = 153$ km s^{-1} at the G band.

The improved depth of this exposure has enabled us to secure a reliable dispersion profile to 26 kpc (circularized), which can be verified independently using both the G band and Fe absorption lines (Figure 2). Spectra of G and K giants from the MILES library (Sánchez-Blázquez et al. 2006) were used to synthesize the optimal stellar template (see Newman et al. 2010). The gain over earlier data is substantial both in extent and sampling. Although $\sigma_{\rm los}(R)$ has been measured to very large radii in local cD galaxies (Kelson et al. 2002), this is to our knowledge the most extended measurement yet obtained in a lensing cluster.

2.4. X-ray

The final ingredient is the mass distribution probed by X-ray emission from the intracluster medium. This was measured by Allen et al. (2008, hereafter A08) using *Chandra* data. Although their analysis assumed spherical symmetry, this has very little effect on the inferred spherically averaged mass profile, as we discuss further in Section 5. Mock observations of simulated clusters show that non-thermal sources of pressure cause X-ray-derived masses to be biased by $\simeq -10\%$ (Nagai et al. 2007; Lau et al. 2009). To account for this, we place a Gaussian prior on $m_{\rm X} \equiv M_{\rm HSE}/M_{\rm true} = 0.9 \pm 0.1$, where $M_{\rm HSE}$ represents the A08 results and $M_{\rm true}$ the true spherically averaged mass distribution. The 10% uncertainty in $m_{\rm X}$ reflects the cluster-to-cluster scatter in non-thermal support, as well as uncertainty in the *Chandra* temperature calibration (Reese et al. 2010). From the A08 mass profile, we take five points spaced log-uniformly from 50 to 600 kpc to match the number of independent temperature measurements. (The results are not sensitive to the inner limit.) Finally, we add 10% in quadrature to the uncertainty in each data point to allow for systematic errors with radial gradients (e.g., non-thermal pressure and errors arising from non-sphericity).

3. DERIVING THE MASS DISTRIBUTION

Our model of the cluster mass distribution comprises three components: (1) the cluster-scale halo, (2) stellar mass in the BCG, and (3) mass in other cluster galaxies which are incorporated as perturbations in the lensing analysis. The third component is modeled as described in our previous work, including two individually modeled galaxies (P1 and P2 in Figure 1). Following N09, the cluster halo and BCG are described by generalized Navarro–Frenk–White (gNFW) and dual pseudoisothermal ellipsoid (dPIE) profiles, with a key improvement: the newly incorporated X-ray data allow us to consider triaxial mass models.

By combining X-ray and lensing constraints, we can directly measure the elongation of the DM distribution along the line of sight (l.o.s.), thus addressing a key systematic uncertainty in deriving the mass density profile. Whereas lensing probes the projected mass contained in cylinders (2D), the X-ray data are sensitive to the spherically averaged (3D) enclosed masses (e.g., Morandi et al. 2010). The combination thus provides information on the l.o.s. geometry. Since the surface density of A383 and the BCG isophotes are both nearly circular ($b/a \simeq 0.9$), any large departure from sphericity must be along the l.o.s.

In detail, we adopt a triaxial gNFW form for the DM halo:

$$\rho_{\rm DM}(r_{\epsilon,\rm DM}) = \frac{1}{q_{\rm DM}} \frac{\rho_0}{(r/r_s)^{\beta}(1+r/r_s)^{3-\beta}}, \quad (1)$$

where

$$r_{\epsilon,\rm DM}(x,y,z) = \sqrt{(1-\epsilon_{\Sigma,\rm DM})x^2 + (1+\epsilon_{\Sigma,\rm DM})y^2 + (z/q_{\rm DM})^2}. \quad (2)$$

[4] http://www.oamp.fr/cosmology/lenstool/

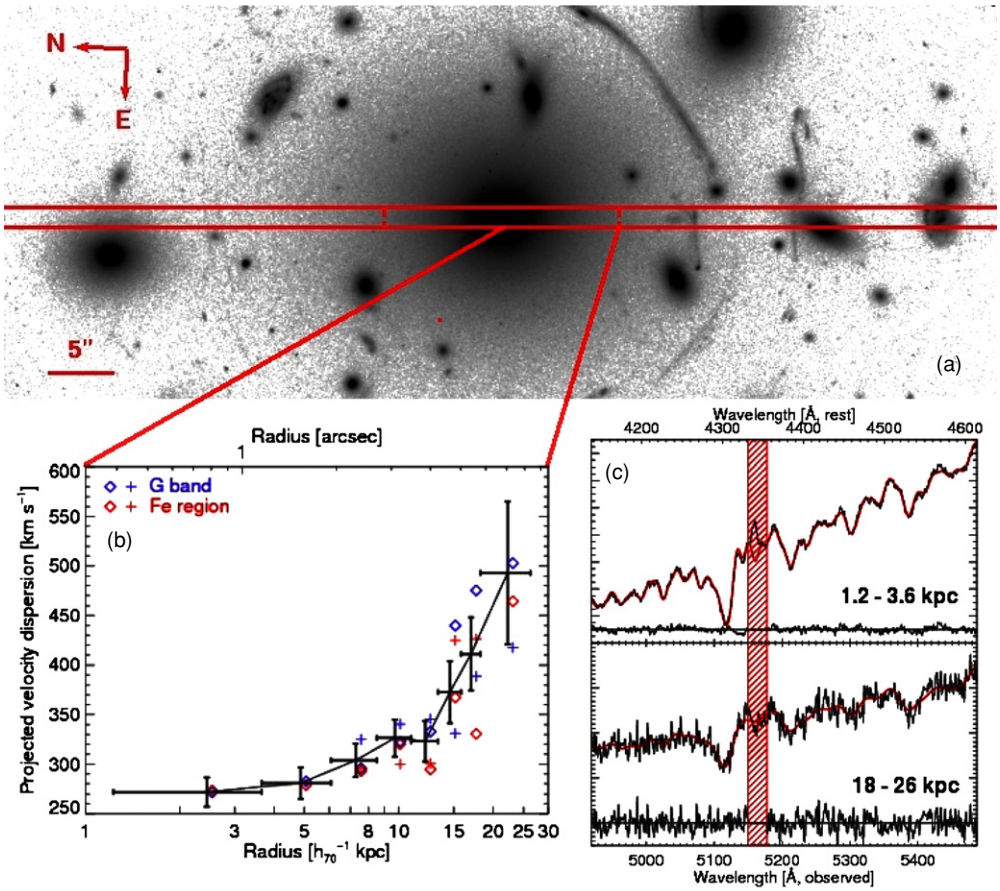

Figure 2. Considerably improved kinematic data for the central galaxy. (a) Long-slit configuration for the 22.8 ks LRIS exposure; the 8.″8 radial extent over which velocity dispersions could be derived is indicated by the vertical red line. (b) Averaged stellar velocity dispersion profile as derived independently from the *G* band and Fe λ5270 absorption line regions (blue and red symbols) on either side of the center (diamond and plus symbols). The rapid rise in the velocity dispersion at large radii due to the DM halo is clearly evident. (c) Spectra for the inner- and outermost spatial bins around the *G* band. Red curves show the fits to the broadened stellar template, with residuals plotted below.

Here, the z-axis is the l.o.s.; the factor $1/q_{\rm DM}$ in Equation (1) therefore ensures that the surface density is constant as $q_{\rm DM}$ varies. The ellipticity of the mass surface density $\epsilon_{\Sigma,{\rm DM}}$ is related to that of the lensing potential $\epsilon_{\phi,{\rm DM}}$ following Golse & Kneib (2002). Note that $q_{\rm DM} > 1$ and <1 correspond to prolate and oblate cases, respectively.

Following N09, the stellar mass of the BCG is modeled by a dPIE profile (Elíasdóttir et al. 2007) fit to *Hubble Space Telescope* (*HST*) surface photometry. However, we consider a more general triaxial deprojection, with $r_{\epsilon,*}$ defined as in Equation (2), replacing $\epsilon_{\Sigma,{\rm DM}}$ and $q_{\rm DM}$ by $\epsilon_{\Sigma,*}$ and q_*, respectively.

Before describing our detailed analysis, it is useful to gain some physical insight into the effects of varying $q_{\rm DM}$ and q_*. $q_{\rm DM}$ governs the ratio between 2D and 3D halo masses and is therefore well constrained by the combination of lensing and X-ray data. In contrast, q_* is not constrained by long-slit kinematic data, and we therefore adopt a prior distribution based on knowledge of the intrinsic axis ratios of elliptical galaxies (Tremblay & Merritt 1995). We can expect that $1 < q_* < q_{\rm DM}$ (in the prolate notation), both because simulated DM halos are much more flattened ($\langle c/a\rangle \simeq 0.5$; Jing & Suto 2002) than stars in elliptical galaxies ($\langle c/a\rangle \simeq 0.7$; Tremblay & Merritt 1995), and because isotropic dissipation processes in the baryon-dominated regime should yield rounder mass distributions (e.g., Abadi et al. 2010). Qualitatively, we expect that for a fixed halo, rounder stellar orbits will enclose less mass, thereby reducing the observed stellar velocity dispersion. This introduces a degeneracy between q_* and β. By accounting for this degeneracy, we incorporate uncertainties arising from triaxiality and projection into our final results.

Technically, models are compared to the X-ray data by computing spherically enclosed masses in a triaxial mass distribution, as justified in Sections 2.4 and 5. Fully triaxial dynamical models are not computationally feasible. However, since the observations imply DM axis ratios of $x : y : z \simeq 1 : 1.1 : 2$, a spheroidal treatment with the symmetry axis along the l.o.s. is a very good approximation. This represents a significant improvement over our previous spherical dynamical models. By assuming a two-integral distribution function $f(E, L_z)$, the dynamics can be computed as described by Gavazzi (2005) and Qian et al. (1995).

Table 1 summarizes the model parameters and our assumed priors. As detailed in N09, models are proposed by Markov Chain Monte Carlo, and their likelihood is computed as the product of the likelihoods of the four data sets.

4. RESULTS: A TRIAXIAL MODEL WITH SHALLOW INNER SLOPE

Our model fits are plotted in Figure 3 and summarized in Table 1. To reconcile the observed velocity dispersions with the

Table 1
Models Inferred from Strong and Weak Lensing, Kinematic, and X-ray Data

Quantity	Units	Prior	Marginalized Posterior
gNFW DM halo			
$\epsilon_{\phi,\rm DM}$	···	[0, 0.15]	$0.055^{+0.017}_{-0.014}$
Position angle (P.A.)	deg	[−10, 30]	$10.5^{+7.6}_{-5.7}$
r_s	kpc	Log-uniform[a]	112^{+61}_{-30}
$\sigma_{0,\rm DM}$	km s^{-1}	Log-uniform[a]	1629^{+150}_{-125}
β	···	Uniform[a]	$0.59^{+0.30}_{-0.35}$
$q_{\rm DM}$	···	[1.5, 2.7]	$1.97^{+0.28}_{-0.16}$
BCG stellar mass			
$r_{\rm core}$, $r_{\rm cut}$ (dPIE)	kpc	0.82, 40.5	(Fixed)
b/a	···	0.88	(Fixed)
P.A.	deg	15	(Fixed)
$M_*/L_{\rm V}$	$(M/L_{\rm V})_\odot$	[1,8]	$3.85^{+0.90}_{-1.19}$
q_*	···	$1/q_*^2 \sim 0.54 \pm 0.15$	$1.30^{+0.15}_{-0.13}$
Calibration parameters			
$m_{\rm WL}$	···	0.81 ± 0.04	$0.78^{+0.03}_{-0.02}$
$m_{\rm X}$	···	0.90 ± 0.10	$1.01^{+0.04}_{-0.05}$
Cluster galaxy perturbers			
$\sigma_{0,*}$	km s^{-1}	159 ± 40	122^{+18}_{-17}
$r_{\rm cut,*}$	kpc	[20, 80]	†
$r_{\rm cut,P1}$	kpc	[20, 120]	†
$r_{\rm cut,P2}$	kpc	[20, 80]	†

Notes. Posteriors are summarized using the mode and the 68% confidence interval. These priors were found to be non-restrictive following initial tests with broader priors. $[a, b]$ denotes a uniform prior, while $\mu \pm \sigma$ denotes a Gaussian, which is truncated at 1.5σ for calibration parameters. The prior on q_* is a fit to Tremblay & Merritt (1995). Formulae to convert σ_0 to other quantities are given in N09. $\sigma_{0,*}$ and $r_{\rm cut,*}$ denote dPIE parameters for an L_* cluster galaxy (see N09). Perturber radii marked with † have nearly flat posteriors, which are omitted.

[a] In practice, independent, uniform priors are placed on linear combinations of $(\log r_s, \log \sigma_{0,\rm DM}, \beta)$ for efficiency; these are equivalent to broad, uniform priors on $\log r_s$, $\log \sigma_{0,\rm DM}$, and β.

lensing and X-ray data, shallow DM slopes are preferred. As expected, the formal uncertainties are increased with respect to previous models that neglected triaxiality (Sand et al. 2008), yet we still obtain $\beta < 0.70$ (68% confidence, <1.0 at 95%). Interestingly, the DM halo is found to be elongated along the l.o.s., with $q_{\rm DM} \sim 2$, typical of simulated halos (Jing & Suto 2002) and consistent with the orientation selection bias expected for strong lenses. Furthermore, the stellar mass-to-light ratio is found to be in agreement with the values inferred from stellar population synthesis models, assuming a Salpeter initial mass function (IMF; Treu et al. 2010).

The parameter degeneracies are illustrated in Figure 4. It is instructive to see how they have been minimized by the combination of observational tools unique to our method. By including only lensing constraints, for example, we would obtain weaker constraints on β due to the unconstrained stellar mass. The degeneracy with r_s is reduced using weak lensing and X-ray probes at large radii. Finally, the DM l.o.s. ellipticity $q_{\rm DM}$ is determined by the combination of X-ray and lensing data.

Equally important to the inferred model parameters is the "goodness of fit." As Figure 3 clearly shows, a relatively simple model, with a single DM halo characterized by a simple functional form, fits all the data remarkably well, including the extended velocity dispersion data and the detailed strong lensing features. (The best-fitting models have image plane rms errors of 0.″3.) The velocity dispersion profile is particularly

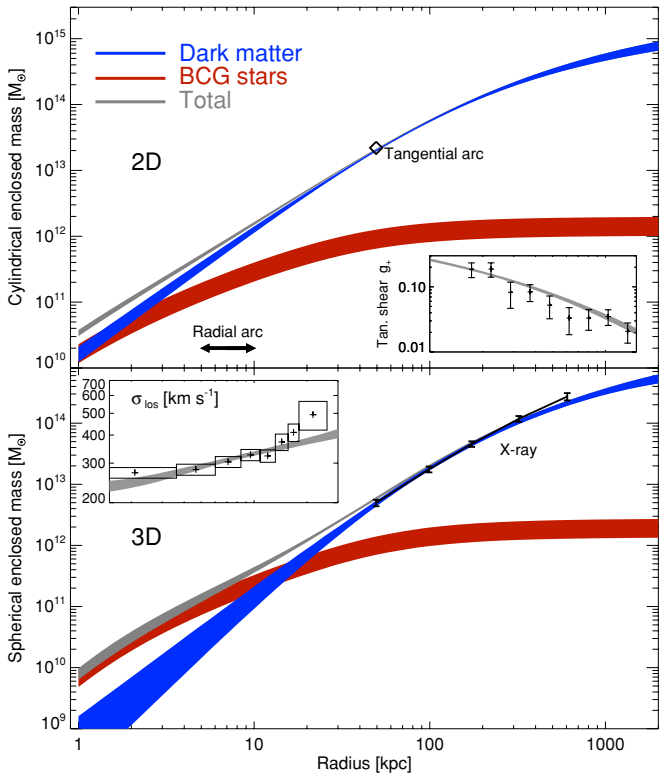

Figure 3. Top: mass enclosed in cylinders (2D) for the dark and stellar components, as well as the total mass distribution, with tangential reduced shear (g_+) data inset at the same radial scale. Bottom: mass enclosed in spheres (3D), with velocity dispersion data inset and X-ray constraints overlaid. All bands show 68% confidence regions. The models acceptably fit all constraints from ≃2 kpc to ≃1.5 Mpc.

encouraging: its shape and normalization are well matched, which was typically challenging using spherical dynamical models (Sand et al. 2008; N09).

5. REMAINING UNCERTAINTIES

In this Letter, we have incorporated additional data and more sophisticated models to address the impact of projection. Here we consider the residual systematic uncertainties. First, we repeated the analysis with all $\sigma_{\rm los}$ measurements shifted by 10% to account for systematic measurement uncertainties. We note that the mild radial orbital anisotropy typically observed at lower redshift can only decrease β (see N09).

Second, we assumed that the BCG is coincident with the center of the DM halo, consistent with the $\lesssim$3 kpc projected offset required by the lensing. A similar 3D offset has little effect on the enclosed mass outside ≃6 kpc, so we can evaluate the effects of this assumption by excluding data within 6 kpc.

A spatially constant M_*/L was assumed, consistent with our non-detection of a color gradient outside the central ≃1″. Following Kelson et al. (2002), we estimate limits on $\Delta M_*/L$ from those on $\Delta(B - R)$. We translate this to an uncertainty on R_e and repeat the analysis shifting R_e.

Finally, we recall that the A08 X-ray measurements assumed sphericity, whereas our mass models are non-spherical. By calculating the gas emission in a non-spherical halo with $q_{\rm DM} = 2$, we estimate that spherically deprojecting the X-ray observables biases the inferred (spherically averaged) mass profile by only ≃7% typically, consistent with previous studies (Gavazzi 2005; Nagai et al. 2007). As discussed in Section 2.4, this small bias is comparable to other systematic

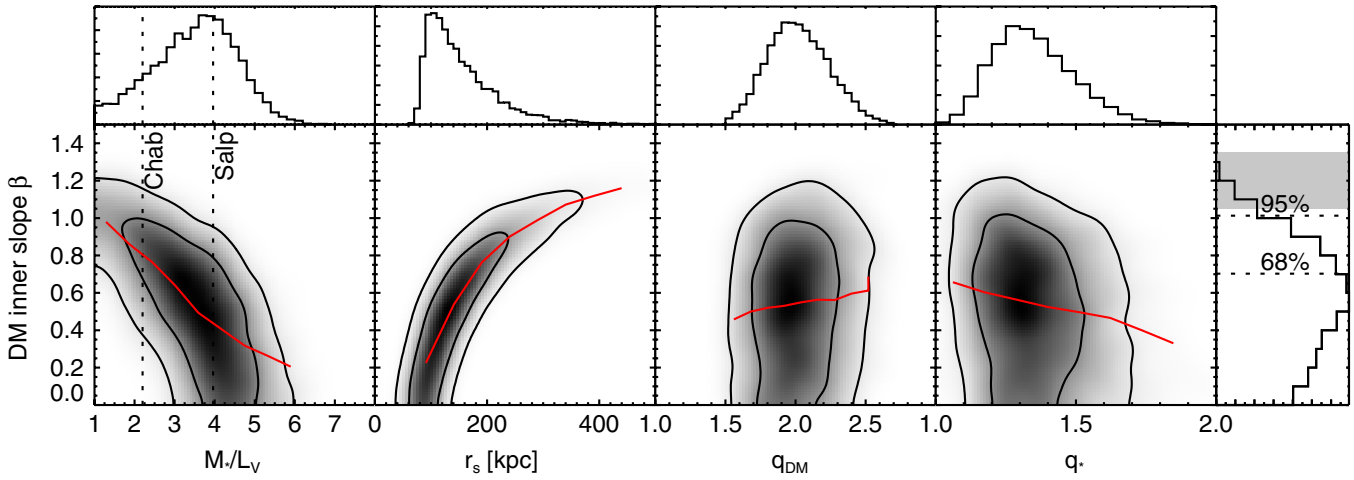

Figure 4. Joint posterior probability density of β with four other model parameters: M_*/L_V, r_s, $q_{\rm DM}$, and q_*. The potential degeneracies are reduced by the inclusion of complementary constraints. Contours show 68% and 95% confidence regions, and red lines indicate the mean β to highlight the degeneracy slopes. Histograms show marginalized posteriors. Upper limits on β are indicated in the right panel, along with the range (shaded) reported for cluster-scale N-body simulations by Diemand et al. (2005). Dotted lines in the left panel show the M_*/L_V inferred from *Subaru* photometry using `kcorrect` (Blanton & Roweis 2007), assuming Chabrier and Salpeter IMFs.

uncertainties inherent to X-ray analyses and is within our adopted calibration uncertainty. We estimate the impact on our results by shifting the X-ray masses accordingly.

In all cases, the limits on β shifted by <0.06. We conclude that the remaining known systematic uncertainties are much smaller than the projection uncertainty addressed in this Letter.

6. DISCUSSION

The shallow inner DM slope we find in A383 is difficult to reconcile with results from numerical simulations. DM-only N-body simulations predict $\beta \simeq 1$–1.3. (e.g., Diemand et al. 2005). Although recent galaxy-scale simulations have suggested continuous, modest flattening (Stadel et al. 2009; Navarro et al. 2010), this is unlikely to affect our comparison, since the slope becomes shallower than NFW only on very small scales ($\lesssim 0.015 r_s \approx 4$ kpc) that encompass only the innermost velocity dispersion bin; this datum does not dominate our results.

Cosmological hydrodynamical simulations incorporating baryonic physics (cooling and feedback) with high resolution find that baryon condensation in the cluster core steepens the DM slope (an effect termed "adiabatic contraction"), thereby increasing β and worsening the discrepancy with observations (e.g., Gnedin et al. 2004, $\beta \simeq 2$; Duffy et al. 2010, $\beta \simeq 1.5$; Sommer-Larsen & Limousin 2010, $\beta \simeq 1.1$). The amount of steepening depends on the details of the subgrid implementation, but the sign of the effect is consistent.

Interestingly, recent hydrodynamical simulations at the galaxy and dwarf galaxy scales have shown that baryons can soften DM cusps (e.g., Governato et al. 2010; Romano-Díaz et al. 2009); however, the relevant processes appear not to scale to galaxy clusters, which have deeper potential wells than dwarf galaxies and are less baryon-dominated than L_* galaxies. Processes that have been suggested to counteract adiabatic contraction in cluster cores, such as a late dry merging (Gao et al. 2004) or dynamical friction by infalling baryonic clumps (El-Zant et al. 2001, 2004; Nipoti et al. 2004), are apparently subdominant in cosmological hydrodynamical simulations and do not lead to a shallow cusp with $\beta < 1$. Our results on shallow DM cusps in galaxy clusters thus seem to require a revision of our understanding of either the DM backbone or the most relevant baryonic physics for shaping the cluster core.

7. SUMMARY

We have extended our previous analyses of A383 by incorporating weak lensing and X-ray data. Based on deep Keck spectroscopic observations, we have also measured—for the first time in a lensing cluster—an extended velocity dispersion profile that demonstrates a clear rise in the outer regions in response to the cluster potential. As a result of these improved data sets, we have refined our modeling to consider triaxial mass distributions. We demonstrate that all four observational ingredients are essential to obtain a complete 3D view of A383 over a very wide dynamic range of three decades in radius.

We find that the DM distribution in A383 is clearly triaxial, consistent with ΛCDM numerical simulations. However, its DM profile has a shallow density cusp with $\beta < 1$ (95%), a result that appears inconsistent with numerical simulations of clusters in a ΛCDM context at moderate significance. Although A383 represents only a single well-studied cluster, comparable data are currently in hand to extend this analysis to a sample of nine clusters whose ensemble properties will be presented in a forthcoming paper.

It is a pleasure to thank Steve Allen for providing his X-ray analysis and to acknowledge the helpful assistance of Eric Jullo, Johan Richard, Jean-Paul Kneib, and Satoshi Miyazaki. We thank the referee, Marceau Limousin, for his constructive suggestions. R.S.E. acknowledges financial support from DOE grant DE-SC0001101. Research support by the Packard Foundation is gratefully acknowledged by T.T. The authors recognize and acknowledge the cultural role and reverence that the summit of Mauna Kea has always had within the indigenous Hawaiian community. We are most fortunate to have the opportunity to conduct observations from this mountain.

REFERENCES

Abadi, M. G., Navarro, J. F., Fardal, M., Babul, A., & Steinmetz, M. 2010, MNRAS, 407, 435
Allen, S. W., Rapetti, D. A., Schmidt, R. W., Ebeling, H., Morris, R. G., & Fabian, A. C. 2008, MNRAS, 383, 879
Benítez, N. 2000, ApJ, 536, 571
Blanton, M. R., & Roweis, S. 2007, AJ, 133, 734
Diemand, J., Zemp, M., Moore, B., Stadel, J., & Carollo, C. M. 2005, MNRAS, 364, 665

Duffy, A. R., Schaye, J., Kay, S. T., Dalla Vecchia, C., Battye, R. A., & Booth, C. M. 2010, MNRAS, 405, 2161
Elíasdóttir, Á., et al. 2007, arXiv:0710.5636
El-Zant, A. A., Hoffman, Y., Primack, J., Combes, F., & Shlosman, I. 2004, ApJ, 607, L75
El-Zant, A., Shlosman, I., & Hoffman, Y. 2001, ApJ, 560, 636
Gao, L., Loeb, A., Peebles, P. J. E., White, S. D. M., & Jenkins, A. 2004, ApJ, 614, 17
Gavazzi, R. 2005, A&A, 443, 793
Ghigna, S., Moore, B., Governato, F., Lake, G., Quinn, T., & Stadel, J. 2000, ApJ, 544, 616
Gnedin, O. Y., Kravtsov, A. V., Klypin, A. A., & Nagai, D. 2004, ApJ, 616, 16
Golse, G., & Kneib, J.-P. 2002, A&A, 390, 821
Governato, F., et al. 2010, Nature, 463, 203
Jing, Y. P., & Suto, Y. 2002, ApJ, 574, 538
Jullo, E., Kneib, J.-P., Limousin, M., Elíasdóttir, Á., Marshall, P. J., & Verdugo, T. 2007, New J. Phys., 9, 447
Kelson, D. D., Zabludoff, A. I., Williams, K. A., Trager, S. C., Mulchaey, J. S., & Bolte, M. 2002, ApJ, 576, 720
Lau, E. T., Kravtsov, A. V., & Nagai, D. 2009, ApJ, 705, 1129
Massey, R., et al. 2007, MNRAS, 376, 13
Morandi, A., Pedersen, K., & Limousin, M. 2010, ApJ, 713, 491
Nagai, D., Vikhlinin, A., & Kravtsov, A. V. 2007, ApJ, 655, 98
Navarro, J. F., Frenk, C. S., & White, S. D. M. 1996, ApJ, 462, 563
Navarro, J. F., et al. 2010, MNRAS, 402, 21
Newman, A. B., Ellis, R. S., Treu, T., & Bundy, K. 2010, ApJ, 717, L103
Newman, A. B., Treu, T., Ellis, R. S., Sand, D. J., Richard, J., Marshall, P. J., Capak, P., & Miyazaki, S. 2009, ApJ, 706, 1078
Nipoti, C., Treu, T., Ciotti, L., & Stiavelli, M. 2004, MNRAS, 355, 1119
Qian, E. E., de Zeeuw, P. T., van der Marel, R. P., & Hunter, C. 1995, MNRAS, 274, 602
Reese, E. D., Kawahara, H., Kitayama, T., Ota, N., Sasaki, S., & Suto, Y. 2010, ApJ, 721, 653
Richard, J., Pei, L., Limousin, M., Jullo, E., & Kneib, J. P. 2009, A&A, 498, 37
Romano-Díaz, E., Shlosman, I., Heller, C., & Hoffman, Y. 2009, ApJ, 702, 1250
Sánchez-Blázquez, P., et al. 2006, MNRAS, 371, 703
Sand, D. J., Treu, T., Ellis, R. S., Smith, G. P., & Kneib, J.-P. 2008, ApJ, 674, 711
Sand, D. J., Treu, T., Smith, G. P., & Ellis, R. S. 2004, ApJ, 604, 88
Smith, G. P., Kneib, J., Smail, I., Mazzotta, P., Ebeling, H., & Czoske, O. 2005, MNRAS, 359, 417
Smith, G. P., & Taylor, J. E. 2008, ApJ, 682, L73
Sommer-Larsen, J., & Limousin, M. 2010, MNRAS, 408, 1998
Springel, V., Frenk, C. S., & White, S. D. M. 2006, Nature, 440, 1137
Stadel, J., Potter, D., Moore, B., Diemand, J., Madau, P., Zemp, M., Kuhlen, M., & Quilis, V. 2009, MNRAS, 398, L21
Tremblay, B., & Merritt, D. 1995, AJ, 110, 1039
Treu, T., Auger, M. W., Koopmans, L. V. E., Gavazzi, R., Marshall, P. J., & Bolton, A. S. 2010, ApJ, 709, 1195